Condensed Matter Physics, 2020, Vol. 23, No 3, 33701: 1–11
DOI: 10.5488/CMP.23.33701
http://www.icmp.lviv.ua/journal

CONDENSED MATTER PHYSICS

Total energy calculation for the metallic hcp phase of Zn in the bulk, layered, and quantum dot limits

D. Olguín*

Centro de Investigación y de Estudios Avanzados del Instituto Politécnico Nacional–Unidad Querétaro, Libramiento Norponiente No. 2000, Fracc. Real de Juriquilla 76230, Santiago de Querétaro, Querétaro, México

Received November 12, 2020, in final form February 12, 2020

The structural and electronic properties of the metallic hcp phase of Zn in the bulk, monolayer, bilayer, and quantum dot limits have been studied by using total energy calculations. From our calculated density of states and electronic band structure, in agreement with previous work, bulk hybridization of the Zn–4s, 3p, and 3d orbitals is obtained. Furthermore, we found that this orbital hybridization is also obtained for the monolayer, bilayer, and quantum dot systems. At the same time, we found that the Zn monolayer and bilayer systems show electronic properties characteristic of lamellar systems, while the quantum dot system shows the behavior predicted for a 0D system.

Key words: *ab initio calculations, metallic Zn, quantum dots, 2D systems*

1. Introduction

The study of the electronic properties of quantum dots (QDs) is very interesting for both basic and applied physics. Small enough quantum dots can contain a few atoms, and their energy spectra are expected to behave like those of "big artificial atoms", showing discrete energy levels [1]. To the best of our knowledge, the electronic and optical properties of semiconductor quantum dots have been summarized in early and recent interesting reviews found in the literature [2–5]. By contrast, for metallic quantum dots, a lack of work is evident. However, important reviews, mainly on metallic clusters, can be found in [6–11].

Metallic quantum dots, in their nanocomposite form, have been proposed for use in memory devices [12, 13] and in coloring glasses. By using the multicolor detection properties of semiconductors, optical devices applicable in nanoscience and nanotechnology, as well as in chemistry, biology, and medicine, can be developed [14–24]. As far as we know, metallic Zn quantum dots have not been studied or reported in the recent scientific literature. However, it is found that Zn clusters were studied recently, where the reports show stable Zn clusters having different stacking arrangement of the atoms as well as interesting electronic properties [25–30]. On the other hand, there is an increasing interest in different Zn-based nanoparticles, the same for biomaterials, as well as in solid state physics, and other technological applications [31–36]. Therein, it has been showed that by using controlled conditions several Zn-based nanocrystals, passivated or dopped, can be grown in the symmetric zinc-blende phase [37–41]. It is also interesting to note the report stating that at low temperature the system $ZrZn_2$ shows ferromagnetic and superconductor properties [42, 43].

Although, no reports on Zn metallic nanocrystals are known, recent work on Zn nanodisks [44–47] showed that Zn metallic nanodisks, with sizes of 520 nm wide and 144 nm thick, can exhibit a mixture of metallic and semiconductor properties [44]. Thus, with the aim of contributing to the study of the electronic properties of metallic quantum dots, in this work, we present the study of the electronic band

*Permanent address: Departamento de Física, Centro de Investigación y de Estudios Avanzados del Instituto Politécnico Nacional, C.P. 07300, Ciudad de México, México

structure of metallic Zn quantum dots. For completeness, calculations for the bulk and layered systems (monolayer and bilayer cases) are also presented. To show the stability of the systems studied, we have calculated the cohesive energy, and our found values will be presented below.

Much of the theoretical work on modelling the quantum dots has been done under the assumption that the finite thickness of a quantum dot, usually much smaller than the lateral extension of the confinement, can be neglected. However, the typical size of a quantum dot ranges from a few Angstroms to micrometers [1, 5]. A complete analysis of the electronic properties of QDs requires the study of their behavior as a function of the QD size. However, these additional calculations, which require considerable computational resources, are outside the scope of the present work.

The remainder of this paper is organized as follows. Section 2 describes the computational strategy used in our calculations. In section 3, a discussion of our results on the calculated cohesive energies and electronic properties for the systems studied is presented. Finally, section 4 presents our conclusions.

2. Calculation method

In our calculations, we used the full-potential linearized augmented plane-wave method (FP-LAPW) as implemented in the WIEN2K code [48]. In this method, wave functions, charge density, and potential are expanded in spherical harmonics within non-overlapping muffin-tin spheres, while plane waves are used in the remaining interstitial region of the unit cell. In the code, the core states are treated with a multiconfiguration relativistic Dirac-Fock approach, whereas valence states are treated in a scalar relativistic approach. The exchange-correlation energy is calculated using the GGA correction of Perdew et al. [49, 50]. The atomic electronic configuration used was Zn [Ar] $4s$ $3d$; where the Zn $3p$ states were treated as valence-band states using the local orbital extension of the LAPW method [48].

To find the minimum of the total energy for each system as a function of the variational parameters, the muffin-tin radius and the cutoff energy, a very careful step analysis was performed, where for the bulk case a value of 11.0 for $R_{\mathrm{MT}}K_{\mathrm{max}}$ (where R_{MT} is the muffin-tin radius and K_{max} is the plane wave cutoff) and a value of 13.0 Ry for the cutoff energy parameter (G_{max}) were used, while for the monolayer case the values used were 10.5 for $R_{\mathrm{MT}}K_{\mathrm{max}}$ and 13.0 Ry for G_{max}, and for the bilayer case the values used were $R_{\mathrm{MT}}K_{\mathrm{max}}$=10.5 and G_{max}=14.0 Ry.

At the same time, in our calculations, an appropriate set of **k**-points in the irreducible sector of the Brillouin zone was used. Here, we used a value of 1600 k-points for the bulk case, equivalent to a $(15 \times 15 \times 7)$ Monkhorst-Pack grid of the unit cell, and 2000 k-points for the layer systems, equivalent to $(20 \times 20 \times 4)$ Monkhorst-Pack grid [51]. It should be noted that for the quantum dots, the variational parameters used for the total energy and electronic calculations were $R_{\mathrm{MT}}K_{\mathrm{max}}$=7.0, G_{max}=12.0 Ry, and only the Gamma point of the first Brillioun zone was used [52, 53].

To study the Zn low dimensional systems, we used the slab model. Therein, for the monolayer case, one Zn-atomic layer in the hcp lattice was constructed, while for the bilayer case, we used two Zn-atomic layers in the hcp lattice keeping the bulk hcp distance between the Zn layers, and for the QD we used a finite slab containing thirteen atomic sites having obtained a pyramidal QD type, whose dimensions were 5.32 Å for the basis and 2.65 Å for the height. Here, we passivated the Zn-QD with Hydrogen atoms, since it had been showed that the passivation stabilizes the bare QD [53]. In the inset of figures 3 and 5, the slab models used are shown schematically, where we can distinguish the different atomic sites for metallic hcp Zn (red symbols).

To properly isolate each slab from their periodic images and to avoid large vacuum zones, which, in plane-wave methods, considerably increase the demand of computational resources, i.e., to keep the calculations accessible, based on the fact that in bulk hcp zinc, the nearest neighbor distances range between 2.66 Å and 2.91 Å for the in-plane and interlayer neighbors, respectively, a vacuum of 10 Å with the upper slab was considered for the layered systems, whereas a vacuum of 13 Å for the upper side and 8 Å for the lateral side was used for the QD system.

3. Results

Before a detailed discussion of the electronic properties of Zn systems, we first show our calculated structural properties of the bulk crystal. The Zn hexagonal crystal structure is showed in the inset of

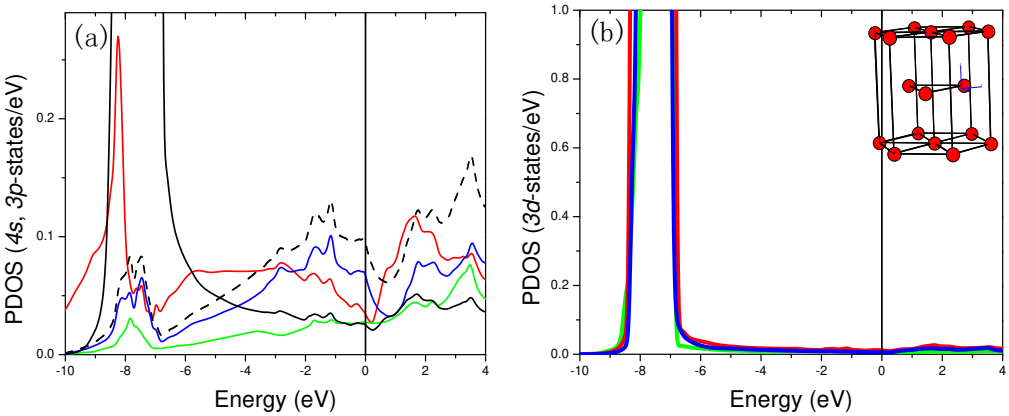

Figure 1. (Color online) The calculated partial density of states (PDOS) for metallic hcp Zn. The left-hand side panel shows the $4s$ (red lines), $3(p_x + p_y)$ (blue lines) and $3p_z$ (green lines) orbitals; for comparison, the $3p$ obitals (black dashed lines), and the $3d$ orbitals (black lines) are also shown. The right-hand side panel shows the $3d_{z^2}$ (green lines), $3(d_{x^2+y^2} + d_{xy})$ (red lines), and $3(d_{xz} + d_{yz})$ (blue lines) orbitals; the inset shows the hcp unit cell. The zero of the energies represents the Fermi level.

figure 1. Our calculated lattice parameters are $a = 2.6712$ Å and $c = 4.9586$ Å. In excelent agreement with the experimental values: $a = 2.6649$ Å and $c = 4.9468$ Å [54].

Then, for the layered systems we relaxed the atomic positions in the slab using the Hellmann-Feynman forces until the force component was less than 0.5 mRy/au. Our results show that, for the monolayer case, the geometry is rigid and does not allow displacements for the in-plane nearest neighbor distances, and for the bilayer case we found that the interlayer distances slightly increase from 2.93 Å (the bulk value) to 2.98 Å. Meanwhile, for the QD case, the system relaxes from 2.93 Å to 2.90 Å, and the in-plane nearest neighbor distances remain almost constant, where the initial and final values are 2.66 Å and 2.67 Å, respectively. In order to show the trend in the stability of the layered systems, we calculated the cohesive energy[55]

$$E_{\text{coh}} = \frac{N_{\text{Zn}} E_i^{\text{free}} - E_{\text{Tot}}^{\text{supercell}}}{N_{\text{Zn}}},$$

where, E_i^{free} is the total energy of the free i-th atom, N_{Zn} the number of Zn atoms in the layer system, and $E_{\text{Tot}}^{\text{supercell}}$ the total energy of the supercell. We found that the cohesive energy for the bilayer case is 0.73 eV/atom, while for the monolayer case the cohesive energy is 0.56 eV/atom.

To calculate the cohesive energy for the hydrogen passivated quantum dot, we need to compute the binding energy

$$E_{\text{binding}} = N_{\text{Zn}} E_{\text{Zn}}^{\text{free}} + N_{\text{H}} E_{\text{H}}^{\text{free}} - E_{\text{Tot}}^{\text{QD}},$$

and then, by removing the Zn-H energy energy from the binding energy, we will have the cohesive energy for the QD [56, 57], i.e.,

$$E_{\text{coh}}^{\text{QD}} = \frac{E_{\text{binding}} + \mu_{\text{H}} N_{\text{H}}}{N_{\text{Zn}}},$$

where μ_{H} is the hydrogen chemical potential. From this expression, we find that the cohesive energy for the QD is 0.29 eV/atom. Considering the relatively low values for the cohesive energies, we found that our calculated systems could be considered stable with weak chemical bonds. Thus, from the experimental point of view, special attention will be necessary to study these systems.

3.1. Electronic properties: Zn bulk

Figure 1 shows the calculated partial density of states (PDOS) for the bulk hcp Zn. For the sake of clarity, the left-hand panel shows the Zn–$4s$ and $3p$ orbitals, while the right-hand panel shows the Zn–$3d$

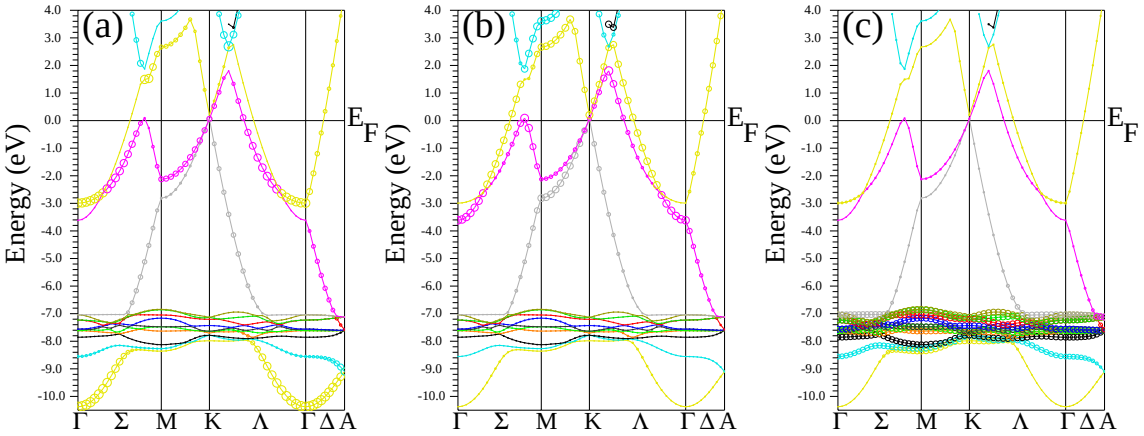

Figure 2. (Color online) The calculated atomic orbital contributions to the electronic band structure of bulk hcp Zn, where the orbital character of the electronic bands is represented by circles (colors are a guide to the eye). The left-hand panel shows the 4*s* orbitals, the middle panel shows the 3*p* orbitals, and the right-hand panel shows the 3*d* orbitals.

orbitals. The plot shows that there is a non-zero population of states at the Fermi level, that is, we have obtained a system with metallic characteristics, as expected.

From the plot, we can distinguish three energy regions where the calculated states are located: below E_F, the first region with energies from −10.5 to −6.7 eV, where the main contribution to the PDOS arises from the 3*d* orbitals; states that are mainly located in the energy range from −8.5 eV to −6.7 eV; a second range of energies from −2.9 eV to 0.0 eV; and a third energy region located above E_F, with energies ranging from 1.6 eV to 3.6 eV.

From the left-hand side panel and from the comparison of the different calculated states shown, we can observe the already known hybridization of the Zn–4*s*, 3*p*, and 3*d* orbitals, in good agreement with earlier work [58–61].

A detailed analysis of the calculated PDOS shows that, in addition to the highly localized $3d_{z^2}$ (green lines), the $3(d_{x^2+y^2}+d_{yx})$ (red lines), and the $3(d_{xz}+d_{yz})$ orbitals (blue lines), the bands whose peaks are located at −8.25 eV have important contributions from the 4*s* orbitals. The main peaks for the $3(p_x + p_y)$ orbitals (blue lines) are located in the energy ranges from −8.13 eV to −7.45 eV and from −2.9 eV to 0.0 eV, as well as at energies above E_F, from 1.6 eV to 3.6 eV. The contributions of the $3p_z$ orbitals (green lines) are obtained at −7.8 eV and 3.5 eV.

Further information on the calculated electronic states can be obtained from the analysis of the atomic orbital contributions to the electronic band structure, as shown in figure 2, where the atomic orbital contributions to the electronic band structure are depicted by circles. A larger circle size corresponds to a higher charge within the atomic sphere, qualitatively showing those orbitals that constitute each electronic band [48].

Figure 2 (a) shows that the lower band located in the energy range from −10.5 eV to −8.0 eV, showing high dispersion, originates from the 4*s* states (yellow circles) and hybridizes with the 3*d* orbitals. Figure 2 (a) and figure 2 (b) show that in the energy range from –7.0 eV to 3.0 eV, the electronic bands are a hybridization of the 4*s* and 3*p* states (magenta and gray circles). Figure 2 (c) shows that the 3*d* orbitals are mainly localized in the energy range from −8.5 eV to −6.7 eV, as we have commented above.

3.2. Zn-monolayer case and Zn-bilayer case

Figure 3 shows our calculated PDOS for the layered systems, where the upper panel depicts the results for the Zn-monolayer case and the lower panel depicts those for the Zn-bilayer case. As in the bulk case, we see that both systems have metallic characteristics.

At the same time, our results show three energy regions where the calculated states are located. Two of these energy regions are below E_F, the lower one in the energy range from approximately −9.2 eV to

−6.8 eV, where the 3*d* states are located, and the second one in the energy range from −6.4 eV to 0.9 eV, where the 4*s* and 3*p* states are located. Above E_F, a third energy range from 0.9 eV to 3.4 eV is obtained, where a second set of 4*s* and 3*p* states is located.

Using the bulk values as a reference, a detailed comparison of the calculated energies for the layered systems shows that the 3*d* states are located in the energy range from −8.5 (−9.2) eV to −6.2 (−6.8) eV (where the first values refer to the monolayer case and the values in parentheses correspond to the bilayer case), almost at the same energy values already found for the bulk case.

By contrast, the calculated values for the 4*s* and 3*p* states move up slightly in energy. For example, the main peak of the lower 4*s* bands is now located at −7.7 (−7.8) eV. Furthermore, a second peak for the 4*s* bands is obtained at −6.8 (−6.8) eV; although this band is also present in the bulk case, it is more noticeable in the layered cases. Additionally, in the energy range from −6.4 eV to 0.6 eV, a new shape of the 4*s* orbitals is obtained; here, these states change from a constant step-like form to a sawtooth form (compare with figure 1). At energies above E_F we obtain three peaks arising from the 4*s* states, one peak located at 1.3 (1.3) eV, another located at 1.8 (1.8) eV, and a third located at 2.5 eV. For comparison, note that in the bulk case, only one band is obtained, namely, the one located at 1.6 eV.

The 3*p* orbitals also changed in shape compared with the bulk case; here, the contribution of the $3(p_x + p_y)$ orbitals (blue lines) to the PDOS in the energy range from −7.7 (−7.6) eV to −6.8 (−7.2) eV seems to be remarkable. There are other noticeable peaks at −0.8 (−1.6) eV and −0.3 (−0.8) eV along with the other peaks in the conduction band at 0.7 (0.8) eV, 1.8 (1.8) eV, and 2.5 (1.8) eV. The contributions of

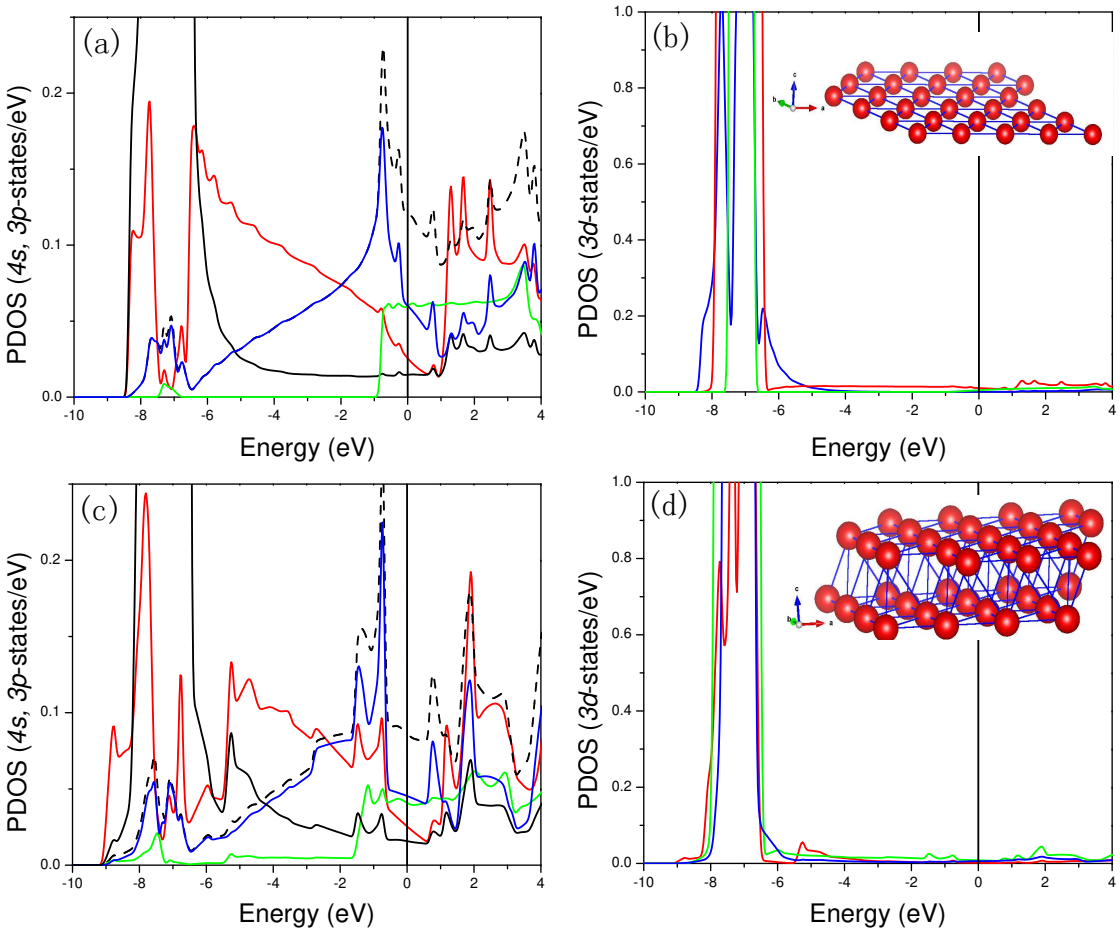

Figure 3. (Color online) Same as figure 1 but for the Zn-monolayer case, upper panel, and the Zn-bilayer case, lower panel. The inset in the right-hand panel shows a schematic of the slab model used in our calculations.

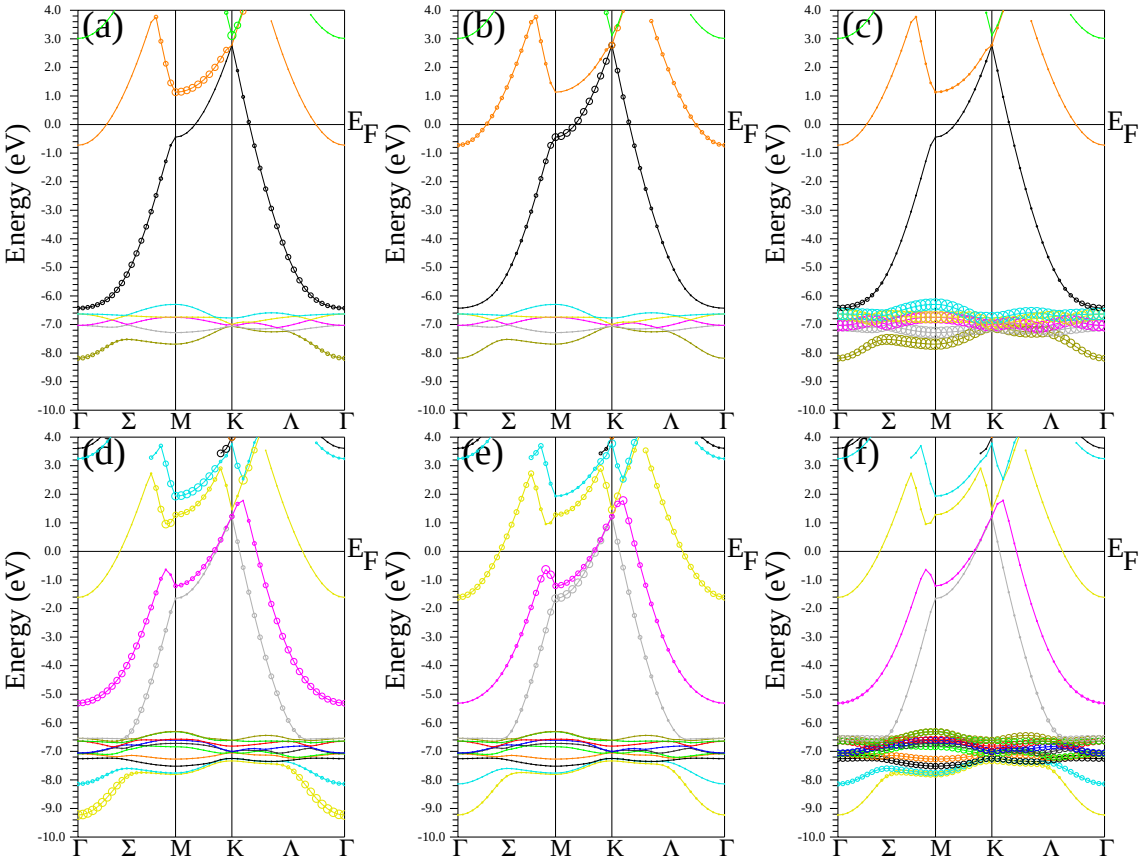

Figure 4. (Color online) Same as figure 2 but for the Zn monolayer (upper panel) and bilayer (lower panel) cases.

the $3p_z$ orbitals (green lines) are obtained at the energy range from −1.5 eV to 3.3 eV, showing a step-like shape at these energies.

The obtained changes in the PDOS can also be observed from the calculated atomic orbital contributions to the electronic band structure, as shown in figure 4, where, due to the different coordination in the apical direction between the layered and bulk cases, the number of bands obtained for the monolayer case is half that for the bilayer and bulk cases.

The calculated energy differences for the $4s$ and $3p$ states can be summarized as follows: in the layered cases, the $4s$ states located in the energy range from −8.5 (−9.3) eV to −7.3 (−7.3) eV show less dispersion than those in the bulk case. Additionally, in the energy range from −6.4 (−7.0) eV to 0.0 eV, the calculated energy values at the high symmetry points move up in energy for the layered systems (compare figure 2 and figure 4).

Finally, we conclude that, except for the differences in the calculated energy values, in general, the calculated electronic properties of the layered systems show a pattern similar to that found for the bulk case, revealing that the in-plane coordination produces lamellar systems, an interesting property of several 2D systems that are the object of recent and intensive work [62–68].

3.3. Zn quantum dot

Figure 5 shows the calculated PDOS for the hydrogen-passivated Zn quantum dot case. For the different peaks associated with the energies found, both below and above E_F, the PDOS shows the structure predicted for a box-like quantum dot [69–72], namely, a delta function behavior; i.e., our results show the effects of quantum confinement [73].

Furthermore, as a consequence of the atomic electronic configuration used in our calculations and

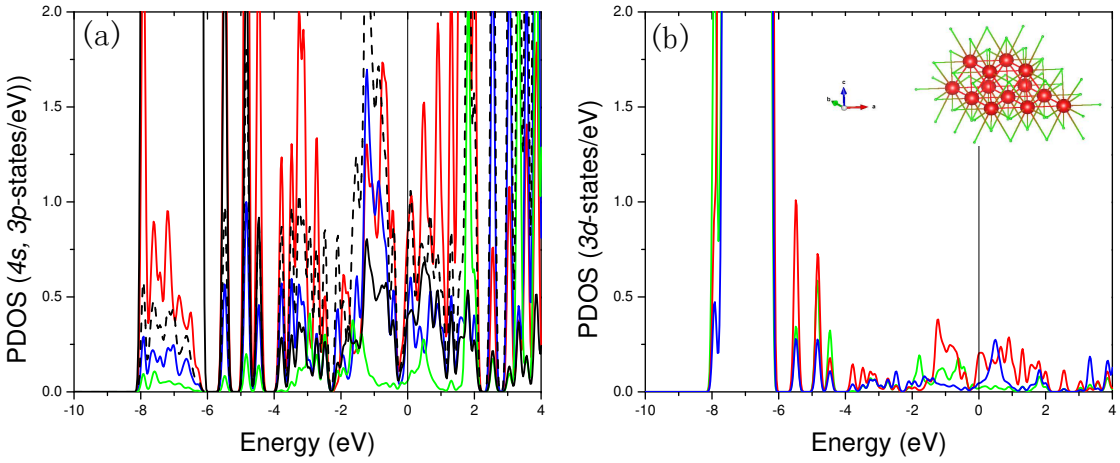

Figure 5. (Color online) Same as figure 1 but for Zn QDs. The inset in the right-hand side panel depicts a schematic representation of the slab used in our calculations, arranged in the Zn hcp phase, which consist of 13 Zn atoms and 48 H atoms (red and green symbols, respectively).

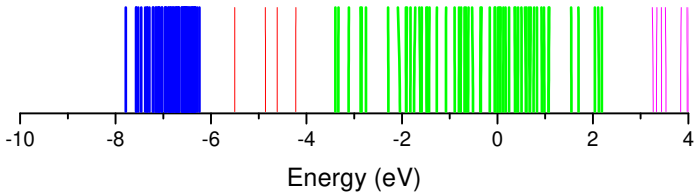

Figure 6. (Color online) The calculated electronic bands for hcp Zn QDs. Colors are a guide to the eye.

due to the strong coupling between the atoms that form the QD, the obtained PDOS clearly shows the hybridization of the Zn–4s, 3p, and 3d atomic orbitals.

A detailed analysis of the calculated PDOS shows that although the Zn–3d orbitals are mainly localized in the energy range from −8.2 eV to −6.2 eV, non-negligible contributions of these orbitals to the PDOS over the entire energy range shown in the plot are also found.

At the same time, for the different energies shown, important contributions from the 4s states (red lines) and 3p states (blue and green lines) are also obtained, showing the above-mentioned hybridization of the Zn–4s, 3p, and 3d orbitals.

As in the previous cases, we can use the electronic band structure to complement the analysis of the calculated PDOS. The calculated electronic band structure for the QD case, depicted in figure 6, shows discrete energy levels, which correspond to the atom-like PDOS shown in figure 5. From the plot, it is easy to see how the energy levels are grouped. The lower energy states, located in the energy range from −7.8 to −6.2 eV, correspond to the 3d orbitals that hybridize with the 4s and 3p orbitals. In the energy range from −5.5 to −4.2 eV, we obtain an isolated set of energy levels that correspond mainly to the 4s and 3p states found in the PDOS. In the energy range from −3.4 to 2.2 eV, we obtain a group of 4s and 3p states forming a dense set of energy levels, and the final energy range, from 3.0 eV to 4.0 eV, shows the last set of energy levels, whose main contribution arises from the 3p orbitals.

Although it is found that low-dimensional zinc oxides, zinc chalcogenides, and other zinc-based systems have been more studied than the low dimensional Zn systems [74–79], considering the lack of

information found for the layered systems and metallic quantum dots, we hope that our study will be useful and motivate future work.

At the same time, to avoid speculations and compare our results with new and future data, the same for the layered systems as well as for the quantum dot, more work will be necessary in order to study the convergence of the total energy as a function of the quantum dot size, the hydrogen passivation, surface effects, and other model parameters of the supercell method used.

4. Conclusions

We have studied the electronic properties of the metallic hcp phase of Zn in the bulk and low-dimensional monolayer, bilayer, and quantum dot systems from first-principles calculations. For the bulk case, our results reproduce the previously published data on the structural and electronic properties. For the monolayer and bilayer cases, our results show that the calculated systems produce lamellar systems, an interesting property of novel 2D systems that attracts attention of the scientific community. By contrast, for the quantum dot system, we found that our calculated DOS reproduces the predicted atom-like behavior of 0D systems. Our calculated cohesive energy for the studied systems, namely 0.73 eV/atom for the bilayer case, 0.56 eV/atom for the monolayer case, and 0.29 eV/atom for the QD, show that although our calculated values are smaller the systems are stable. Considering the interest in and prospects for application of the different layered systems as well QDs, we hope that our work motivates future research on these and other non-traditional metallic low-dimensional systems.

Acknowledgements

Computational resources from ABACUS-Cinvestav, Conacyt grant EDOMEX-2011-COI-165873, and Xiuhcoatl-Cinvestav are gratefully acknowledged.

References

1. Kastner M.A., Phys. Today, 1993, **46**, 24–31, doi:10.1063/1.881393.
2. Lehtonen O., Sundholm D., Vänskä T., Phys. Chem. Chem. Phys., 2008, **10**, 4535–4550, doi:10.1039/b804212h.
3. Boxberg F., Tulkki J., Rep. Prog. Phys., 2007, **70**, 1425–1471, doi:10.1088/0034-4885/70/8/R04.
4. Zwanenburg F.A., Dzurak A.S., Morello A., Simmons M.Y., Hollenberg Ll.C.L., Klimeck G., Rogge S., Coppersmith S.N., Eriksson M.A., Rev. Mod. Phys., 2013, **85**, 961–1019, doi:10.1103/RevModPhys.85.961.
5. Reimann S.M., Manninen M., Rev. Mod. Phys., 2002, **74**, 1283–1342, doi:10.1103/RevModPhys.74.1283.
6. Brack M., Rev. Mod. Phys., 1993, **65**, 677–732, doi:10.1103/RevModPhys.65.677.
7. Cheshnovsky O., Taylor K.J., Conceicao J., Smalley R.E., Phys. Rev. Lett., 1990, **64**, 1785–1788, doi:10.1103/PhysRevLett.64.1785.
8. De Heer W.A., Rev. Mod. Phys., 1993, **65**, 611–676, doi:10.1103/RevModPhys.65.611.
9. Furche F., Ahlrichs R., Weis P., Jacob C., Gilb S., Bierweiler T., Kappes M.M., J. Chem. Phys., 2002, **117**, 6982–6990, doi:10.1063/1.1507582.
10. Häberlen O.D., Chung S.-Ch., Stener M., Rösch N., J. Chem. Phys., 1997, **106**, 5189–5201, doi:10.1063/1.473518.
11. Taylor K.J., Pettiette-Hall C.L., Cheshnovsky O., Smalley R.E., J. Chem. Phys., 1992, **96** 3319–3329, doi:10.1063/1.461927.
12. Lin C.W., Pan T.S., Chen M.C., Yang Y.J., Tai Y., Chen Y.F., App. Phys. Lett., 2011, **99**, 023303, doi:10.1063/1.3605596.
13. Jin Z., Liu G., Wang J., AIP Adv., 2013, **3**, 052113, doi:10.1063/1.4804948.
14. Zhang J., Sheng J., Int. J. Hydrogen Energy, 2009, **34**, 3531–3534, doi:10.1016/j.ijhydene.2009.02.032.
15. Hatef A., Sadeghi S.M., Boulais E., Meunier M., Nanotechnol., 2013, **24**, 015502, doi:10.1088/0957-4484/24/1/015502.
16. Kang M., Lee H., Kang T., Kim B., J. Mater. Sci. Technol., 2015, **31**, 573–580, doi:10.1016/j.jmst.2015.01.007.
17. Zhang J., Sheng J., J. Nano Res., 2015, **32**, 66–70, doi:10.4028/www.scientific.net/JNanoR.32.66.

18. Olejnik M., Krajnik B., Kowalska D., Lin G., Mackowski S., J. Phys.: Condens. Matter, 2013, **25**, 194103 (11 pages), doi:10.1088/0953-8984/25/19/194103.
19. Sheng J., Chen S., Zhang J., Li J., Yu J., Int. J. Hydrogen Energy, 2009, **34**, 1119–1122, doi:10.1016/j.ijhydene.2008.10.063.
20. Dražić M.S., Cerovski V.Z., Žikić R., Phys. Status Solidi B, 2014, **251**, 1438–1450, doi:10.1002/pssb.201350243.
21. Shahid R., Muhammad N., Gonfa G., Toprak M.S., Muhammed M., J. Phys. Chem. Solids, 2015, **85**, 34–38, doi:10.1016/j.jpcs.2015.04.020.
22. Dai W., Dong H., Fugetsu B., Cao Y., Lu H., Ma X., Zhang X., 2015, **11**, 4158–4164, doi:10.1002/smll.201500208.
23. Haughn C.R., Steenbergen E.H., Bissell L.J., Chen E.Y., Eyink K.G., Zide J.M.O., Doty M.F., Appl. Phys. Lett., 2014, **105**, 103108, doi:10.1063/1.4895519.
24. Frade T., Melo M.E., Gomes A., Surf. Coat. Technol., 2012, **206**, 3459–3466, doi:10.1016/j.surfcoat.2012.02.012.
25. Piotrowski M.J., Piquini P., Da Silva J.L.F., Phys. Rev. B, 2010, **81**, 155446, doi:10.1103/PhysRevB.81.155446.
26. Wang J., Wang G., Zhao J., Phys. Rev. A, 2003, **68**, 013201, doi:10.1103/PhysRevA.68.013201.
27. Iokibe K., Tachikawa H., Azumi K., J. Phys. B: At. Mol. Opt. Phys., 2007, **40**, 427–436, doi:10.1088/0953-4075/40/2/015.
28. Gutsev G.L., Weatherford C.W., Belay K.G., Ramachandran B.R., Jena P., J. Chem. Phys., 2013, **138**, 164303, doi:10.1063/1.4799917.
29. Aguado A., Vega A., Lebon A., Issendorff B., Nanoscale, 2018, **10**, 19162–19181, doi:10.1039/c8nr05517c.
30. Aguado A., Vega A., Lebon A., Issendorff B., Angew. Chem. Int. Ed., 2015, **54**, 2111–2115, doi:10.1002/anie.201409835.
31. Ali A., Phull A.R., Zia M., Nanotechnol Rev., 2018, **7**, 413–441, doi:10.1515/ntrev-2018-0067.
32. Su Y., Cockerill I., Wang Y., Qin Y.X., Chang L., Zheng Y., Zhu D., Trends Biotechnol., 2018, **37**, 428–441, doi:10.1016/j.tibtech.2018.10.009.
33. Su Y., Wang K., Gao J., Yang Y., Qin Y.X., Zheng Y., Zhu D., Acta Biomater., 2019, **98**, 174–185, doi:10.1016/j.actbio.2019.03.055.
34. Darroudi M., Nasab N.K., Salimizand H., Dehnad A., Nanomed. J., 2019, **6**, 258–262, doi:10.22038/nmj.2019.06.000003.
35. Seyedmajidi S.A., Seyedmajidi M., Moghadamnia A., Haghanifar S., Ziaei R., Zahedpasha S., Halalkhor S., Dent. Res. J., 2014, **11**, 475–480.
36. Cerovic A., Miletic I., Sobajic S., Blagojevic U., Radusinovic M., El-Sohemy A., Biol. Trace Elem. Res., 2007, **116**, 61–71, doi:10.1007/BF02685919.
37. Pal S., Goswami B., Sarkar P., J. Phys. Chem., 2001, **111**, 16072–16075, doi:10.1021/jp074950j.
38. Karanikolos G.N., Alexandridis P., Mountziaris T.J., Mater. Sci. Eng. B, 2008, **152**, 66–71, doi:10.1016/j.mseb.2008.06.028.
39. Goswami B., Pal S., Sarkar P., Seifert G., Springborg M., Phys. Rev. B, 2006, **73**, 205312, doi:10.1103/PhysRevB.73.205312.
40. Goswami B., Pal S., Sarkar P., Phys. Rev. B, 2007, **76**, 045323, doi:10.1103/PhysRevB.76.045323.
41. Christian P., Liu E., Polyhedron, 2010, **29**, 691–696, doi:10.1016/j.poly.2009.10.003.
42. Day C., Phys. Today, 2001, **54**, 16–19, doi:10.1063/1.1420499.
43. Pfleiderer C., Uhlarz M., Hayden S.M., Vollmer R., Löhneysen H.v., Bernhoeft N.R., Lonzarichk G.G., Nature, 2001, **412**, 59–61, doi:10.1038/35083531.
44. Lin J.H., Huang Y.J., Su Y.P., Liu C.A., Devan R.S., Ho C.H., Wang Y.P., Lee H.W., Chang C.M., Liou Y., Ma Y.R., RSC Adv., 2012, **2**, 2123–2127, doi:10.1039/c2ra00972b.
45. López R., Vigueras-Santiago E., Hernández-López S., Acuña P., Argueta-Vega A., Colín-Becerril N., Villa-Sánchez G., Rosales-Dávalos J., Rev. Mex. Fis., 2017, **63**, 308–313.
46. Lin J.H., Patil R.A., Devan R.S., Liu Z.A., Wang Y.P., Ho C.H., Liou Y., Ma Y.R., Sci. Rep., 2014, **4**, 6967, doi:10.1038/srep06967.
47. Devan R.S., Lin J.H., Huang Y.J., Yang Ch.Ch., Wu S.Y., Liou Y., Ma Y.R., Nanoscale, 2011, **3**, 4339–4345, doi:10.1039/c1nr10694e.
48. Blaha P., Schwarz K., Luitz J., WIEN97, Vienna University of Technology, 1997.
49. Perdew J.P., Wang Y., Phys. Rev. B, 1992, **45** 13244–13249, doi:10.1103/PhysRevB.45.13244
50. Perdew J.P., Burke S., Ernwerhof M., Phys. Rev. Lett., 1996, **77** 3865–3868, doi:10.1103/PhysRevLett.77.3865.
51. Monkhorst H.J., Pack J.D., Phys. Rev. B, 1976, **13**, 5188–5192, doi:10.1103/PhysRevB.13.5188.
52. Xi Y., Zhao X., Wang A., Wang X., Bu H., Zhao M., Physica E, 2013, **49**, 52–60, doi:10.1016/j.physe.2013.01.003.

53. Yamijala S.S.R.K.C., Bandyopadhyay A., Pati S.K., Chem. Phys. Lett., 2014, **603**, 28–32, doi:10.1016/j.cplett.2014.04.025.
54. Jette E., J. Chem. Phys., 1935, **3**, 605–616, doi:10.1063/1.1749562.
55. Wang D., Sun Z., Han D., Liu L., Niu L., RSC Adv., 2017, **7**, 11834–11839, doi:10.1039/c7ra00483d.
56. Zdetsis A.D., J. Phys. Chem. C, 2011, **115**, 14507–14516, doi:10.1021/jp2023007.
57. Zdetsis A.D., Koukaras E.N., Garoufalis C.S., Appl. Phys. Lett., 2007, **91**, 203112, doi:10.1063/1.2813019.
58. Daniukt S., Jarlborgj T., Kontrym-Sznajdt G., Majsnerowskit J., Stachowiakt H., J. Phys.: Condens. Matter, 1989, **1**, 8397–8406, doi:10.1088/0953-8984/1/44/011.
59. Singh P.P., Phys. Rev. Lett., 1994, **72**, 2446–2449, doi:10.1103/PhysRevLett.72.2446.
60. Blaha P., Schwarz K., Dederichs P.H., Phys. Rev. B, 1988, **38**, 9368–9364, doi:10.1103/PhysRevB.38.9368.
61. Sha X.W., Papaconstantopoulos D.A., Mehl M.J., Bernstein N., Phys. Rev. B, 2011, **84**, 184109, doi:10.1103/PhysRevB.84.184109.
62. Ullah N., Zhang R.Q., Murtza G., Yar A., Mahmood A., Solid State Comm., 2016, **246**, 54–58, doi:10.1016/j.ssc.2016.07.005.
63. Singh N., Kaloni T.P., Schwingenschögl U., App. Phys. Lett., 2013, **102**, 023101, doi:10.1063/1.4781382.
64. Rudenko A.N., Katsnelson M.I., Phys. Rev. B, 2014, **89**, 201408(R), doi:10.1103/PhysRevB.89.201408.
65. Kaloni T.P., Gangopadhyay S., Singh N., Jones B., Schwingenschögl U., Phys. Rev. B, 2013, **88**, 235418, doi:10.1103/PhysRevB.88.235418.
66. Zhang S., Yan Z., Li Y., Chen Z., Zeng H., Angew. Chem. Int. Ed., 2015, **54**, 3112–3115, doi:10.1002/anie.201411246.
67. Xian L., Pérez Paz Bianco E., Ajayan P.M., Rubio A., 2D Mater., 2017, **4**, 041003 (7 pages), doi:10.1088/2053-1583/aa8418.
68. Zhou J., Sumpter B.G., Kent P.R.C., Huang J., ACS App. Mater. Interfaces, 2015, **7**, 1458–1464, doi:10.1021/am505655m.
69. Arakawa Y., Sakaki H., Appl. Phys. Lett., 1982, **40**, 939–941, doi:10.1063/1.92959.
70. Batabyal R., Dev B.N., Physica E, 2014, **64**, 224–233, doi:10.1016/j.physe.2014.07.017.
71. Lee S.J., Shin N.H., Ko J.J., Parkt M.J., Kiimmel R., Semicond. Sci. Technol., 1992, **7**, 1072–1079, doi:10.1088/0268-1242/7/8/008.
72. Nilius N., Wallis T.M., Ho W., Science, 2002, **297**, 1853–1856, doi:10.1126/science.1075242.
73. Harman T.C., Taylor P.J., Walsh M.P., LaForge B.E., Science, 2002, **297**, 2229–2232, doi:10.1126/science.1072886.
74. Guo C.F., Wang Y., Jiang P., Cao S., Miao J., Zhang Z., Liu Q., Nanotechnology, 2008, **19**, 445710 (8 pages), doi:10.1088/0957-4484/19/44/445710.
75. Azpiroz J.M., Mosconi E., Ugalde J.M., de Angelis F., J. Phys. Chem. C, 2014, **118**, 3274–3284, doi:10.1021/jp409182r.
76. Kumar H., Barman P.B., Singh R.R., Int. J. Sci. Eng. Res., 2014, **5**, No. 5, 40–53.
77. Son D.I., Kwon B.W., Park D.H., Seo W.S., Yi Y., Angadi B., Lee Ch.-L., Choi W.K., Nat. Nanotechnol., 2012, **7**, 465–471, doi:10.1038/NNANO.2012.71.
78. De Queiroz A.A.A., Martins M., Soares D.A.W., Franca E.J., J. Mol. Struct., 2008, **873**, 121–129, doi:10.1016/j.molstruc.2007.03.013.
79. Fang X., Zhai T., Gautam U.K. , Li L., Wu L., Bando Y., Golberg D., Prog. Mater Sci., 2011, **56**, 175–287, doi:10.1016/j.pmatsci.2010.10.001.

Обчислення повної енергії для металічної гексагональної щільноукладеної фази Zn в об'ємі, багатошарових границях і в границі квантової точки

Д. Олгуін

Центр досліджень та підвищення кваліфікації Національного політехнічного інституту — підрозділ Керетаро, м. Сантьяго де Керетаро, Мексика

Досліджено структурні та електронні властивості металічної гексагональної щільноукладеної фази Zn в об'ємі, багатошарових границях і в границі квантової точки, використовуючи обчислення повної енергії. З обчислень густини станів і електронної зонної структури, що узгоджуються з нашими попередніми результатами, отримано об'ємну гібридизацію $4s$, $3p$ і $3d$ орбіталей Zn. Крім того, ми знайшли, що гібридизація орбіталей також отримується для моношарових, двошарових систем і систем з квантовою точкою. Одночасно встановлено, що моношарові і двошарові системи Zn виявляють електронні властивості, характерні для ламеларних систем, в той час, як система квантових точок демонструє поведінку, передбачену для 0D системи.

Ключові слова: *обчислення з перших принципів, металічний Zn, квантові точки, 2D системи*